

2D MoN_{1,2}-rGO Stacked Heterostructures Enabled Water State Modification for Highly Efficient Interfacial Solar Evaporation

Huimin Yu, Deyu Wang, Huanyu Jin, Pan Wu, Xuan Wu, Dewei Chu, Yi Lu, Xiaofei Yang,* and Haolan Xu*

Improving interfacial solar evaporation performance is crucial for the practical application of this technology in solar-driven seawater desalination. Lowering evaporation enthalpy is one of the most promising and effective strategies to significantly improve solar evaporation rate. In this study, a new pathway to lower vaporization enthalpy by introducing heterogeneous interactions between hydrophilic hybrid materials and water molecules is developed. 2D MoN_{1,2} nanosheets are synthesized and integrated with rGO nanosheets to form stacked MoN_{1,2}-rGO heterostructures with massive junction interfaces for interfacial solar evaporation. Molecular dynamics simulation confirms that atomic thick 2D MoN_{1,2} and rGO in the MoN_{1,2}-rGO heterostructures simultaneously interact with water molecules, while the interactions are remarkably different. These heterogeneous interactions cause an imbalanced water state, which easily breaks the hydrogen bonds between water molecules, leading to dramatically lowered vaporization enthalpy and improved solar evaporation rate (2.6 kg m⁻² h⁻¹). This study provides a promising strategy for designing 2D-2D heterostructures to regulate evaporation enthalpy to improve solar evaporate rate for clean water production.

and high photothermal conversion efficiencies, TMNs have also demonstrated potential applications in interfacial solar evaporation,^[8–10] a promising technology for sustainable clean water supply.^[11–18] For example, group 4 TMNs, especially TiN, was initially explored as a photothermal material in solar evaporation due to their strong localized surface plasmon resonance effects.^[19] Molybdenum nitrides (MoN_x) such as MoN and Mo₂N were also investigated and have shown good evaporation performance due to their great photothermal effect.^[9] However, the evaporation rate and energy efficiency of TMNs-based photothermal evaporators still need to be improved to exceed the theoretical limit to target higher clean water yield for practical applications.

Lowering water vaporization enthalpy is an effective strategy to further promote solar evaporation rate with the same energy input.^[20–23] One intensively applied


method is producing porous structure and reducing materials dimension, which increases actual evaporation surface area and thus equivalently reduces evaporation enthalpy and increases evaporation rate.^[24–34] Therefore, preparation of 2D MoN_x nanosheets with a large surface area should be able to improve solar evaporation rate. In addition, hydrophilic groups

1. Introduction

Transition metal nitrides (TMNs) as a kind of MXene analogue have emerged and shown great potential in energy-related applications by virtue of their unique physiochemistry properties.^[1–7] Recently, owing to their broadband solar absorbance

H. Yu, D. Wang, P. Wu, X. Wu, H. Xu
Future Industries Institute, UniSA STEM
University of South Australia
Mawson Lakes Campus, Adelaide, SA 5095, Australia
E-mail: haolan.xu@unisa.edu.au

H. Jin
School of Chemical Engineering and Advanced Materials
University of Adelaide
Adelaide, SA 5005, Australia

 The ORCID identification number(s) for the author(s) of this article can be found under <https://doi.org/10.1002/adfm.202214828>.

© 2023 The Authors. Advanced Functional Materials published by Wiley-VCH GmbH. This is an open access article under the terms of the Creative Commons Attribution-NonCommercial License, which permits use, distribution and reproduction in any medium, provided the original work is properly cited and is not used for commercial purposes.

H. Jin
Institute for Sustainability
Energy and Resources
University of Adelaide
Adelaide, SA 5005, Australia

D. Chu
School of Materials Science and Engineering
University of New South Wales
Sydney, NSW 2052, Australia

Y. Lu, X. Yang
Jiangsu Co-Innovation Center of Efficient Processing and Utilization of Forest Resources
International Innovation Center for Forest Chemicals and Materials
College of Science
Nanjing Forestry University
Nanjing 210037, China
E-mail: xiaofei.yang@njfu.edu.cn

DOI: 10.1002/adfm.202214828

that have strong interactions with water molecules can disturb the hydrogen bonding network of water molecules to increase the content of intermediate water (IW), thus reducing the water vaporization enthalpy.^[20,21] Accordingly, nanoporous hydrogels and carbon foams have been designed to increase the contact between water molecules and hydrophilic groups.^[35–46] Based on this mechanism, it is supposed that atomic thick 2D MoN_x nanosheets with large surface area and massive hydrophilic groups on their surfaces can strongly interact with water molecules to increase the content of IW, thus reducing the water vaporization enthalpy. Apart from the strategy of enhancing hydrophilic surface-water interactions, it is supposed that introducing multiple or heterogeneous interactions between the surfaces and water molecules should be able to boost the distortion of the hydrogen bonding network and lower evaporation enthalpy. However, 2D MoN_x itself cannot induce such heterogeneous interactions. 2D-2D heterostructures formed by stacking two different types of atomic thick 2D materials have shown unique electronic, optoelectronic and catalytic properties due to atomically sharp interfaces and partial electrostatic transparency.^[47–52] Although interactions between water molecules and 2D-2D heterostructures have not been investigated, it is reasonable to assume that different atomic thick 2D components in the heterostructures can simultaneously interact with water molecules while their interactions are remarkably different, which should be beneficial for breaking hydrogen bonding between water molecules and lowering the vaporization enthalpy.

Therefore, in this work 2D MoN_{1.2} nanosheets were synthesized and integrated with reduced graphene oxide (rGO) nanosheets to form 2D heterostructures. Different from Mo₂N and MoN, the MoN_{1.2} exhibits a higher valence state of Mo owing to the higher nitrogen content, leading to better stability and corrosion resistance for practical applications.^[5] Both 2D MoN_{1.2} and rGO are photothermal materials with broad light absorption and excellent light-to-heat conversion effect, ensuring sufficient energy input during interfacial solar evaporation. By adjusting the surface charge of rGO, smaller MoN_{1.2} nanosheets were closely stacked on larger rGO nanosheets to

form the 2D MoN_{1.2}-rGO stacked heterostructures (MoN_{1.2}-rGO-HSs) with massive heterointerfaces (i.e., junction interfaces) (Figure 1). Numerical simulations depicted that both 2D MoN_{1.2} and rGO interacted with water molecules near the surfaces and heterointerfaces of MoN_{1.2}-rGO-HSs. These heterogeneous interactions caused the imbalanced water state, which easily broke hydrogen bonds between water molecules, leading to a dramatic improvement in solar evaporation rate (2.6 kg m⁻¹ h⁻¹), far beyond the theoretical limit (1.46 kg m⁻¹ h⁻¹) for a typical 2D photothermal evaporator.^[23,53–55]

2. Results and Discussion

Initially, 2D MoN_{1.2} nanosheets were synthesized using a molten salt method by annealing MoO₃ and Na₂MoO₄·2H₂O mixture under 5% NH₃ in an Ar atmosphere.^[56] The 2D morphology of the obtained MoN_{1.2} was clearly revealed by scanning electron microscopy (SEM, Figure 2a). X-ray diffraction (XRD) analysis confirmed the hexagonal crystalline structure of the prepared MoN_{1.2} (Figure S1, Supporting Information).^[56] The atomic structure was further investigated by spherical-aberration-corrected scanning transmission electron microscopy (STEM). The atoms exhibited a hexagonal crystalline phase with a lattice space of 0.25 nm, corresponding to (2 $\bar{1}$ 0) and (1 1 0) facets of the MoN_{1.2} (Figure 2b). rGO (Figure S2, Supporting Information) was chosen to load 2D MoN_{1.2} nanosheets to form the 2D MoN_{1.2}-rGO-HSs. However, the stacked 2D heterostructures cannot be established by directly mixing MoN_{1.2} and rGO suspensions due to the electrostatic repulsions between the two negatively charged components (Figure 1). Only dispersed clusters of MoN_{1.2} and rGO nanosheets (denoted as MoN_{1.2}-rGO) were formed (Figure S3, Supporting Information). To solve this problem, poly(diallyldimethylammonium chloride) (PDDA) was first added into the rGO suspension to reverse the surface charge from negative to positive (Figure 1 and Figure 2c). Then, the positively charged MoN_{1.2} and the negatively charged rGO nanosheets formed the stack structures owing to the electrostatic attractions (Figure S4, Supporting

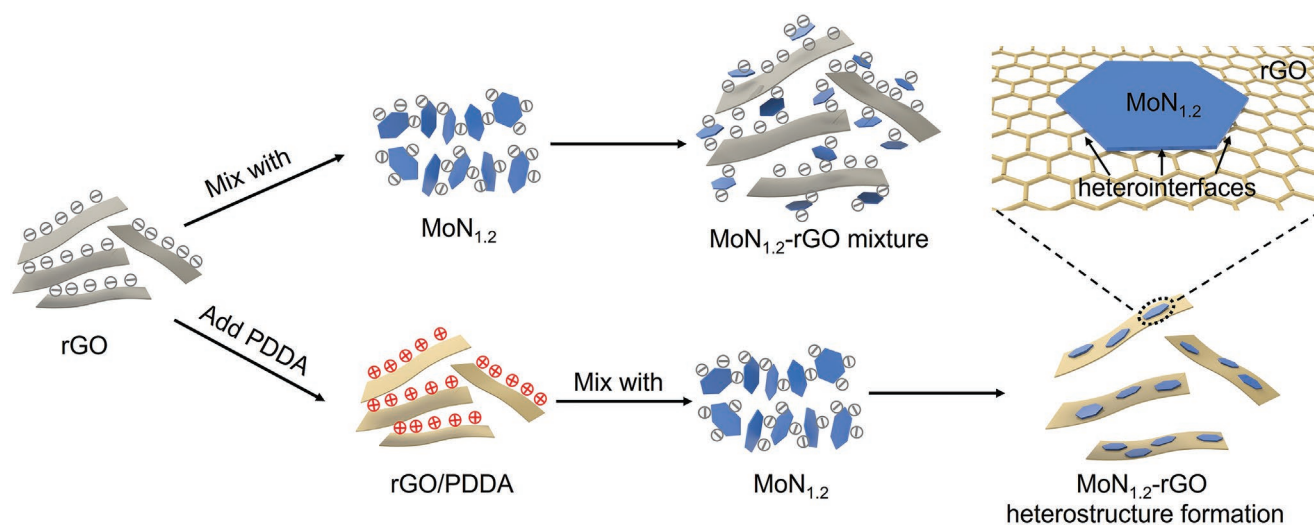


Figure 1. Schematic illustration of the formation of MoN_{1.2}-rGO and MoN_{1.2}-rGO-HSs.

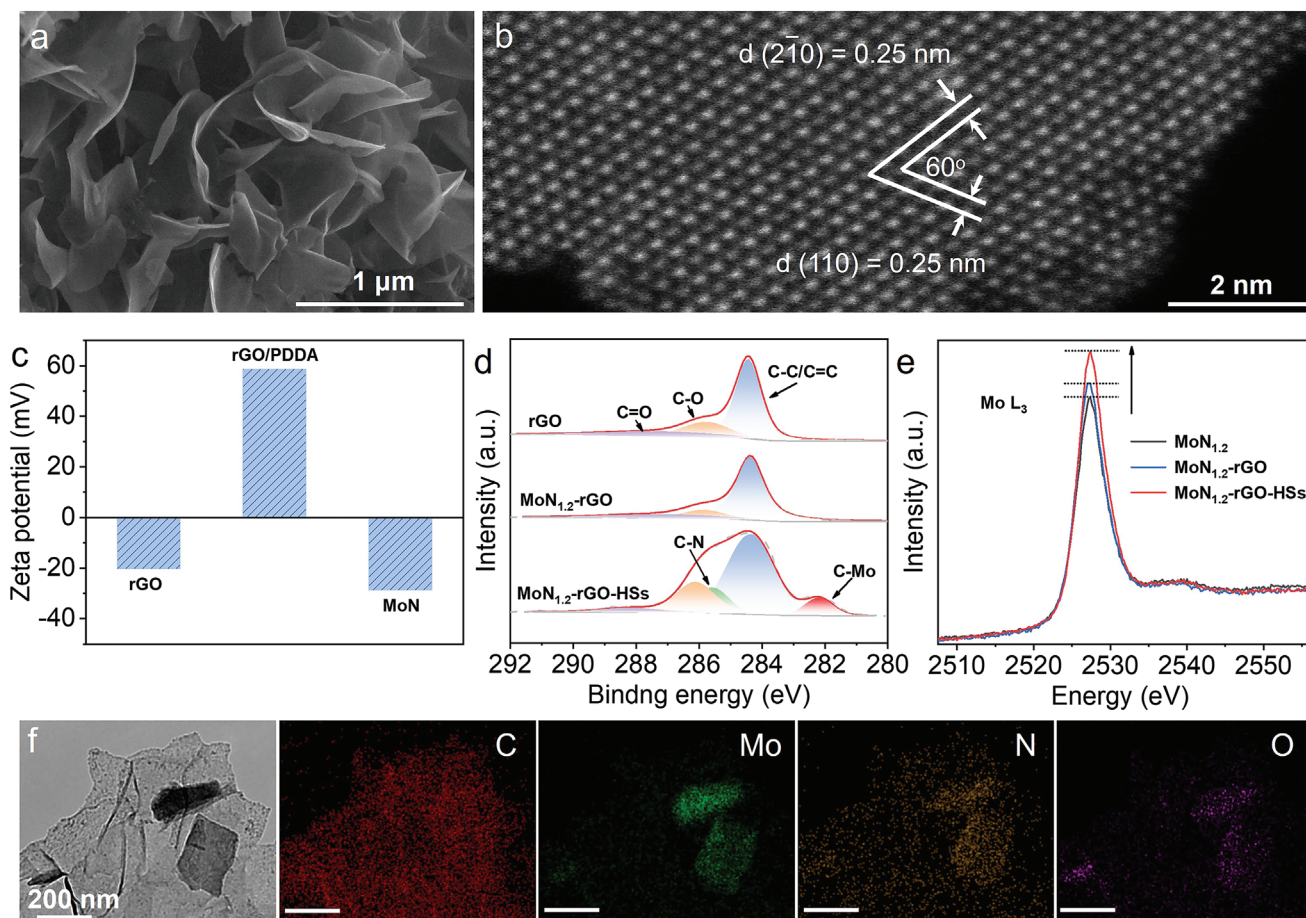


Figure 2. Characterization of the MoN_{1.2}-rGO-HSs. a) SEM image of 2D MoN_{1.2} nanosheets, b) high resolution HAADF-STEM image of a 2D MoN_{1.2} nanosheet, c) zeta potential of rGO, rGO/PDDA, and MoN_{1.2} dispersions, d) C 1s XPS curves of rGO, MoN_{1.2}-rGO, and MoN_{1.2}-rGO-HSs, e) Mo L₃ edge XANES spectra of MoN_{1.2}, MoN_{1.2}-rGO, and MoN_{1.2}-rGO-HSs, f) TEM-EDS elemental mapping of the MoN_{1.2}-rGO HSs.

Information). Once this stacked 2D-2D structures formed, in addition to the electrostatic attractions, strong van der Waals forces between the 2D MoN_{1.2} and rGO nanosheets ensured the stable MoN_{1.2}-rGO heterostructures (also known as van der Waals heterostructures).^[47,49] The full X-ray photoelectron spectroscopy (XPS) survey spectrum showed all C, O, N, and Mo elements (Figure S5, Supporting Information), and the high resolution XPS spectrum elucidated that Mo 3d moved to a higher binding energy after forming MoN_{1.2}-rGO-HSs (Figure S6, Supporting Information). Furthermore, C–Mo bond at 282.2 eV was also directly detected by the high resolution XPS spectrum of C 1s in the 2D stacked heterostructures (Figure 2d). The C–Mo bond was not found in the sample of PDDA modified MoN_{1.2} (Figure S7, Supporting Information), indicating that the C–Mo bond in MoN_{1.2}-rGO-HSs was originated from the direct interactions between rGO and MoN_{1.2}, which confirmed the successful establishment of the closely stacked heterostructures. This finding was further supported by synchrotron-based near-edge X-ray absorption fine structure (NEXAFS) characterization that allowed the investigation of the impact on the surface electronic structures of the *d* electrons. The Mo L-edge white-lines originated from *p* electron transition to a vacant *d* electron state.^[57] According to the Mo-L₃ edge

NEXAFS spectra (Figure 2e), the MoN_{1.2}-rGO-HSs showed the highest intensity of adsorption edge peak, which further confirmed the formation of closely stacked MoN_{1.2}-rGO heterointerfaces. In addition, a lower adsorption edge peak of C-K edge NEXAFS spectra was observed in MoN_{1.2}-rGO-HSs (Figure S8, Supporting Information), in accordance with the XPS results. The stacked 2D structure of MoN_{1.2}-rGO-HSs was clearly observed by SEM (Figure S4, Supporting Information) and TEM (Figure 2f; Figure S9, Supporting Information). Energy-dispersive spectroscopy (EDS) mapping of C, O, N, and Mo elements confirmed that the MoN_{1.2} nanosheets with smaller sizes were in-plane laid on the surface of a large rGO nanosheet to form the MoN_{1.2}-rGO-HSs (Figure 2f).

Photothermal evaporators were prepared by embedding rGO, MoN_{1.2}, MoN_{1.2}-rGO, or MoN_{1.2}-rGO-HSs into Poly(vinyl alcohol) (PVA) hydrogels (denoted as rGO-PVA, MoN_{1.2}-PVA, MoN_{1.2}-rGO-PVA, and MoN_{1.2}-rGO-HSs-PVA hydrogel evaporator, respectively) to investigate their evaporation performances. Unlike the typical method for preparing PVA-based hydrogels with the function of lowering evaporation enthalpy, our method did not require multiple freeze drying-thaw treatments, significantly simplifying the fabrication process. Due to the innate hydrophilic nature of the constituents of PVA

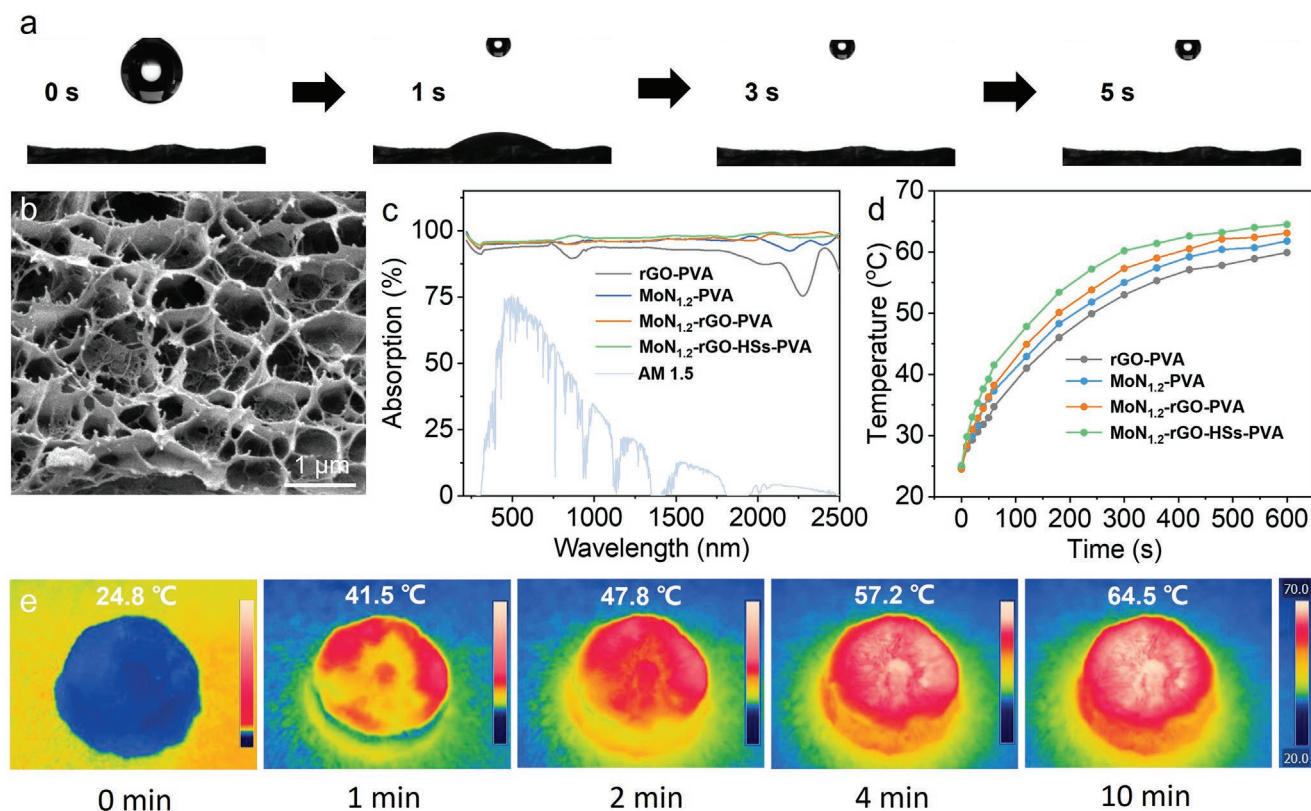


Figure 3. Characterization of the hydrogel evaporators. a) Absorption of a water droplet on the MoN_{1.2}-rGO-HSs-PVA hydrogel surface, b) cross-sectional SEM image of the MoN_{1.2}-rGO-HSs-PVA hydrogel, c) UV-vis-NIR absorption spectra of rGO-PVA, MoN_{1.2}-PVA, MoN_{1.2}-rGO-PVA and MoN_{1.2}-rGO-HSs-PVA hydrogels, d) temperature curves of dry rGO-PVA, MoN_{1.2}-PVA, MoN_{1.2}-rGO-PVA and MoN_{1.2}-rGO-HSs-PVA hydrogels under 1.0 sun illumination, e) IR images of the surface of the MoN_{1.2}-rGO-HSs-PVA hydrogel under 1.0 sun irradiation.

and MoN_{1.2}, the MoN_{1.2}-PVA, MoN_{1.2}-rGO-PVA, and MoN_{1.2}-rGO-HSs-PVA hydrogels showed excellent hydrophilicity as evidenced by the rapid adsorption of a water droplet (5–6 s) during contact angle measurements (Figure 3a; Figure S10b,c, Supporting Information). The rGO-PVA hydrogel showed a slightly slower water droplet adsorption (≈ 9 s) owing to the relatively hydrophobic nature of rGO (Figure S10a, Supporting Information). Vertical water transportation along the MoN_{1.2}-rGO-HSs-PVA hydrogel was also investigated (Figure S11, Supporting Information). When the bottom of the hydrogel was contacted with water, it only took 18 s for water to transport from the bottom to the top surface, ensuring a fast water supply during solar evaporation. The cross-sectional SEM images showed the interconnected porous structure of the hydrogels, which provided channels for efficient water transportation, vapor escape, and salt diffusion during solar evaporation (Figure 3b; Figure S12, Supporting Information). Light absorption of the fabricated hydrogels across UV-vis-NIR regions (220–2500 nm) was measured prior to solar evaporation. As shown in Figure 3c, the hydrogels with MoN_{1.2} showed similar light absorptions of $\approx 96\%$, higher than that of rGO-PVA hydrogel ($\approx 93\%$), indicating higher full-spectrum adsorption of MoN_{1.2} than rGO. The photothermal conversion efficiency of the hydrogels was investigated by monitoring the temperature increase under 1.0 sun illumination in the air (Figure 3d). The dry MoN_{1.2}-rGO-HSs-PVA hydrogel demonstrated a quick

increase in surface temperature from 24.8 to 41.5 °C within 1 min and thereafter reached 64.5 °C at 10 mins (Figure 3e), higher than other hydrogels.

The evaporation performance of the rGO-PVA, MoN_{1.2}-PVA, MoN_{1.2}-rGO-PVA, and MoN_{1.2}-rGO-HSs-PVA hydrogels were initially investigated under 1.0 sun illumination (Figure 4a). MoN_{1.2}-rGO-HSs-PVA hydrogel showed the highest solar evaporation rate of 2.6 kg m⁻² h⁻¹, which was much higher than that of rGO-PVA (1.7 kg m⁻² h⁻¹), MoN_{1.2}-PVA (2.1 kg m⁻² h⁻¹), and MoN_{1.2}-rGO-PVA (2.2 kg m⁻² h⁻¹) evaporators (Figure 4b). The MoN_{1.2}-rGO-HSs-PVA hydrogel demonstrated the lowest average surface temperature of ≈ 37.3 °C (Figure 4c) compared to the rGO-PVA, MoN_{1.2}-PVA, and MoN_{1.2}-rGO-PVA hydrogels (Figure S13, Supporting Information) at steady solar evaporation by virtue of the highest light-to-vapor conversion efficiency, consistent with the best evaporation rate. To investigate the potential contribution of PDDA in MoN_{1.2}-rGO-HSs to solar evaporation, rGO/PDDA-PVA hydrogel was prepared (Note 1, Supporting Information) and compared with rGO-PVA hydrogel. While the hydrogels showed a similar porous structure (Figure S14a, Supporting Information), rGO/PDDA-PVA hydrogel demonstrated better light adsorption compared to the rGO-PVA hydrogel (Figure S14b, Supporting Information). This was attributed to the well-dispersed rGO in PDDA solution, which led to a homogenous distribution of rGO in the hydrogel. The increased light absorption and dispersibility of

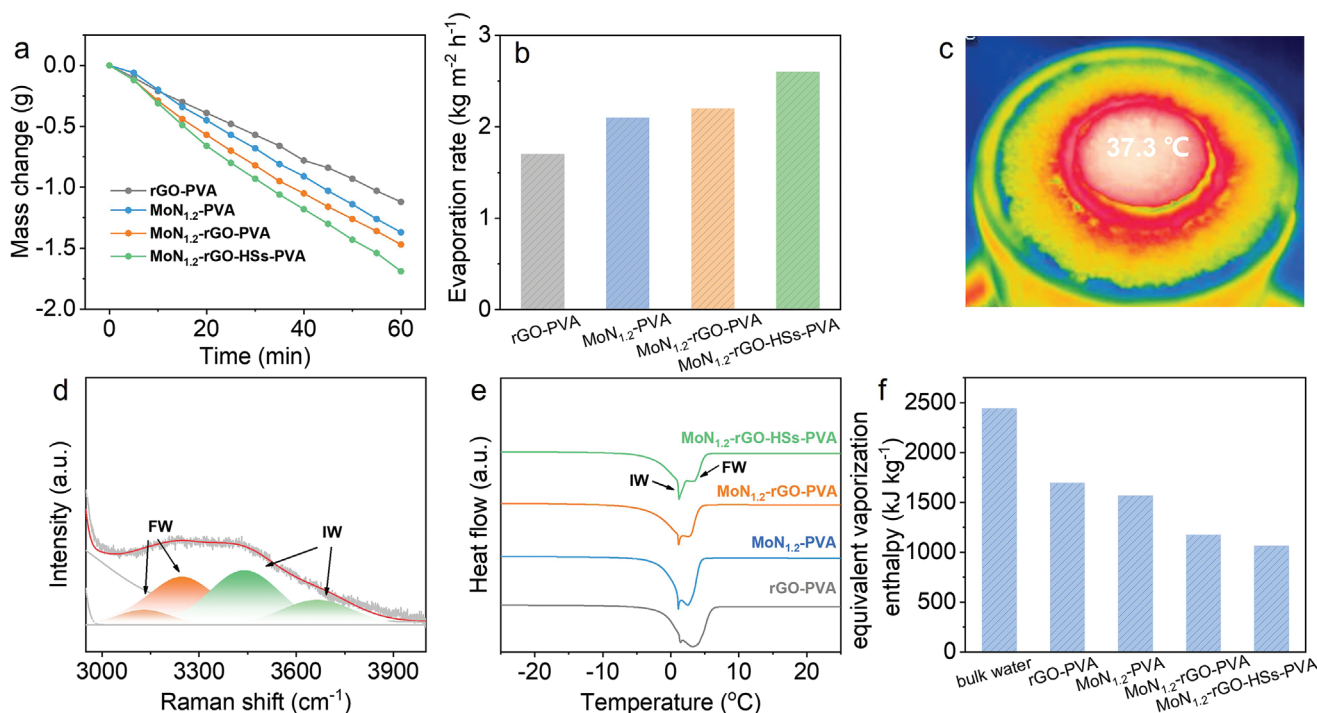


Figure 4. Evaporation performance of the hydrogel evaporators. a) Mass loss of water with rGO-PVA, MoN_{1.2}-PVA, MoN_{1.2}-rGO-PVA and MoN_{1.2}-rGO-HSs-PVA hydrogels under 1.0 sun, b) evaporation rate of rGO-PVA, MoN_{1.2}-PVA, MoN_{1.2}-rGO-PVA and MoN_{1.2}-rGO-HSs-PVA hydrogels, c) IR image of the surface of MoN_{1.2}-rGO-HSs-PVA hydrogel during steady solar evaporation, d) Raman spectrum showing the fitting peaks of IW and FW in MoN_{1.2}-rGO-HSs-PVA hydrogel, e) DSC curves of rGO-PVA, MoN_{1.2}-PVA, MoN_{1.2}-rGO-PVA and MoN_{1.2}-rGO-HSs-PVA hydrogels at fully swollen state, f) equivalent vaporization enthalpy of bulk water and water in rGO-PVA, MoN_{1.2}-PVA, MoN_{1.2}-rGO-PVA and MoN_{1.2}-rGO-HSs-PVA hydrogels.

rGO led to a slightly higher evaporation rate of 1.9 kg m⁻² h⁻¹ for rGO/PDDA-PVA hydrogel (Figure S14c, Supporting Information). In contrast, due to the initial high hydrophilicity and excellent dispersibility of MoN_{1.2}, adding PDDA (i.e., MoN_{1.2}/PDDA-PVA hydrogel) did not increase the evaporation rate (2.1 kg m⁻² h⁻¹) for MoN_{1.2}/PDDA-PVA hydrogel (Note 2 and Figure S15, Supporting Information). These evaporation rates were still much lower than that of MoN_{1.2}-rGO-HSs-PVA hydrogel (2.6 kg m⁻² h⁻¹), indicating that PDDA had limited contribution to the high evaporation rate of MoN_{1.2}-rGO-HSs-PVA hydrogel, while the stacked 2D heterostructure was the key. The long-term stability of the MoN_{1.2}-rGO-HSs-PVA hydrogel was evaluated by 32 cycles (1 h per cycle) of tests over 4 days under one sun illumination (Figure S16, Supporting Information). The MoN_{1.2}-rGO-HSs-PVA hydrogel showed a steady evaporation rate each day. The slight fluctuation in evaporation rate on different days was attributed to the variation in the environmental humidity.^[58,59]

To elucidate the mechanism of enhancing solar evaporation over 2D MoN_{1.2}-rGO stacked heterostructures, water states in the hydrogel were analyzed using Raman spectra (Note 3, Supporting Information). Water constrained within the hydrogel evaporators can be classified into three types according to the different hydrogen bonding: bound water (BW), intermediate water (IW), and free water (FW).^[20] Raman spectrum of the water within the MoN_{1.2}-rGO-HSs-PVA evaporator revealed peaks of FW at ≈3131, ≈3245 cm⁻¹ and IW at ≈3441, ≈3669 cm⁻¹ in the region of O–H stretching (Figure 4d). By calculating

the peak areas of the two types of water, it was found that the ratio of IW to FW was 1.16 for MoN_{1.2}-rGO-HSs-PVA, which was much higher than that of rGO-PVA (0.64), MoN_{1.2}-PVA (0.73), and MoN_{1.2}-rGO-PVA (0.84) hydrogels (Figure S17, Supporting Information), demonstrating the large amount of IW induced by the MoN_{1.2}-rGO heterostructures. The differential scanning calorimetry (DSC) curves further confirmed that the water in MoN_{1.2}-rGO-HSs-PVA showed the highest IW content, consistent with the Raman results (Figure 4e). Since IW involves only weak interactions, higher IW content results in a lower evaporation enthalpy,^[20] leading to a higher evaporation rate with the same energy input. DSC analysis also confirmed the lowest evaporation enthalpy for water in MoN_{1.2}-rGO-HSs-PVA hydrogel (Note 4, Figure S18, Supporting Information). The equivalent water evaporation enthalpy for free bulk water, and water constrained in rGO-PVA, MoN_{1.2}-PVA, MoN_{1.2}-rGO-PVA, and MoN_{1.2}-rGO-HSs-PVA evaporators were measured by dark evaporation experiments (Note 5, Figure S19, Supporting Information), which were 2442, 1696, 1567, 1174, and 1062 kJ kg⁻¹, respectively (Figure 4f). The evaporation enthalpy of water in hydrogels was lower than that of free bulk water, which was mainly attributed to the enlarged evaporation surface area originated from the porous structure of the hydrogel and the disturbance of the hydrogen bonding network due to the interactions between the hydrophilic groups of the hydrogel and water molecules.^[20] Consistent with the Raman and DSC results, the measured evaporation enthalpy of the water in MoN_{1.2}-rGO-HSs-PVA was much lower than

that of water in other three hydrogels, confirming that the 2D MoN_{1.2}-rGO stacked heterostructures activated the water state for faster evaporation. In addition, MoN_{1.2}-rGO-HSs-PVA-1 and MoN_{1.2}-rGO-HSs-PVA-3 with different molar ratios of 2D MoN_{1.2} to rGO (1:3 and 3:1 respectively) were prepared to compare with the MoN_{1.2}-rGO-HSs-PVA (molar ratio of 1:1). The cross-sectional SEM images showed that the MoN_{1.2}-rGO-HSs-PVA-1 and MoN_{1.2}-rGO-HSs-PVA-3 had similar interconnected porous structures (Figure 3b; Figure S20a,b, Supporting Information). The evaporation rates of MoN_{1.2}-rGO-HSs-PVA-1 (2.2 kg m⁻² h⁻¹) and MoN_{1.2}-rGO-HSs-PVA-3 (2.5 kg m⁻² h⁻¹, Figure S20c, Supporting Information) were lower than that of MoN_{1.2}-rGO-HSs-PVA (2.6 kg m⁻² h⁻¹). The measured evaporation enthalpy of water in MoN_{1.2}-rGO-HSs-PVA-1 (1155 kJ kg⁻¹) and MoN_{1.2}-rGO-HSs-PVA-3 (1105 kJ kg⁻¹, Figure S20d, Supporting Information) were higher than that in MoN_{1.2}-rGO-HSs-PVA (1062 kJ kg⁻¹), which explained the lower evaporation rates. It is supposed that the greatest amount of heterostructures in the MoN_{1.2}-rGO-HSs-PVA led to the best evaporation performance.

To gain an in-depth insight into the effect of 2D heterostructures on water evaporation, molecular dynamics simulation (MDS) with universal forcefield was conducted. The stacked 2D MoN_{1.2} and rGO heterointerface was built by placing the (001) facet of MoN_{1.2} on the (001) facet of rGO (Figure S21, Supporting Information), which was in accordance with the TEM results (Figure 2). When locating water molecules on the MoN_{1.2} surface (Figure 5a) or near the heterointerface of MoN_{1.2}-rGO-HS with different distances (Figure 5b,c), the stacked MoN_{1.2} and rGO simultaneously interacted with water molecules, while the two types of interactions varied at different locations (Figure 5d,e,f). Especially when the water molecules were located near the heterointerface (Figure 5b), MoN_{1.2}-water and rGO-water interactions were significantly

different (Figure 5e). These strong heterogeneous interactions would drive water molecules into imbalanced states, which broke the hydrogen bonds between water molecules and thus accelerating the evaporation process.

To mimic water evaporation over different surfaces, rGO (Figure S22, Supporting Information), MoN_{1.2} (Figure S23, Supporting Information), fully overlapped MoN_{1.2}-rGO without exposed heterointerfaces (Figure S24, Supporting Information), and MoN_{1.2}-rGO-HSs with heterointerfaces (Figure S21, Supporting Information) were established. 500 water molecules were placed on their surfaces and evaporated at 375 °C, respectively. The simulated results showed that 52 water molecules were evaporated from the rGO surface at 1000 ps (Figure 6a), which was slightly lower than the water escaped from MoN_{1.2} surface (62 water molecules, Figure 6b). In comparison, much more water molecules (141) escaped from the fully overlapped MoN_{1.2}-rGO surface (Figure 6c), confirming that introducing heterogeneous interactions can remarkably improve the evaporation rate. The loss of water molecules was further increased to 192 by introducing the MoN_{1.2}-rGO heterointerfaces (Figure 6d) to enhance the imbalanced interactions with water molecules. These simulation results confirmed that MoN_{1.2}-rGO-HSs had the best performance in solar evaporation due to the presence of both 2D-2D heterostructures and heterointerfaces, which agreed well with the experimental results.

The performance of MoN_{1.2}-rGO-HSs-PVA hydrogel in real seawater evaporation was also investigated. During 8 h of continuous test under 1.0 illumination, a stable evaporation rate of ≈2.4 kg m⁻² h⁻¹ was delivered (Figure S25a, Supporting Information). The surface of the MoN_{1.2}-rGO-HSs-PVA was kept clear without any salt accumulation during the test (Figure S25a, Supporting Information), indicating excellent salt-resistance performance. This was due to the abundant

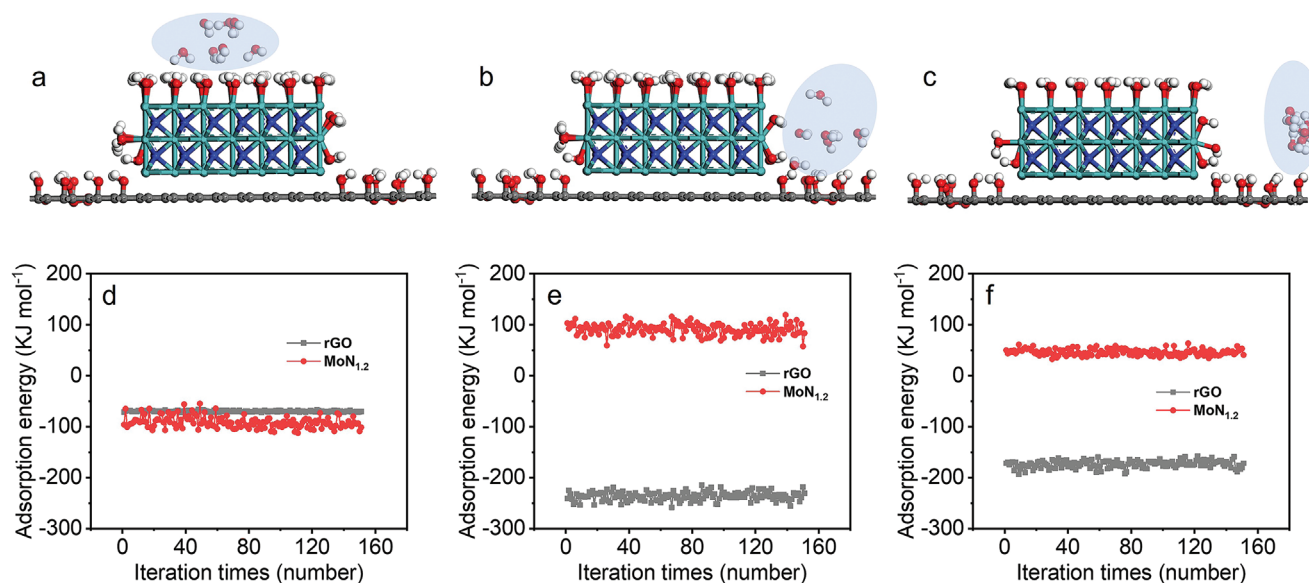


Figure 5. Adsorption energy between MoN_{1.2}-rGO-HS and water molecules at different positions. Water molecules located a) above MoN_{1.2} surface of MoN_{1.2}-rGO-HS, b) near the heterointerface of MoN_{1.2}-rGO-HS, c) above rGO surface of MoN_{1.2}-rGO-HS far away from the heterointerface, and d–f) the corresponding water adsorption energy of MoN_{1.2} and rGO.

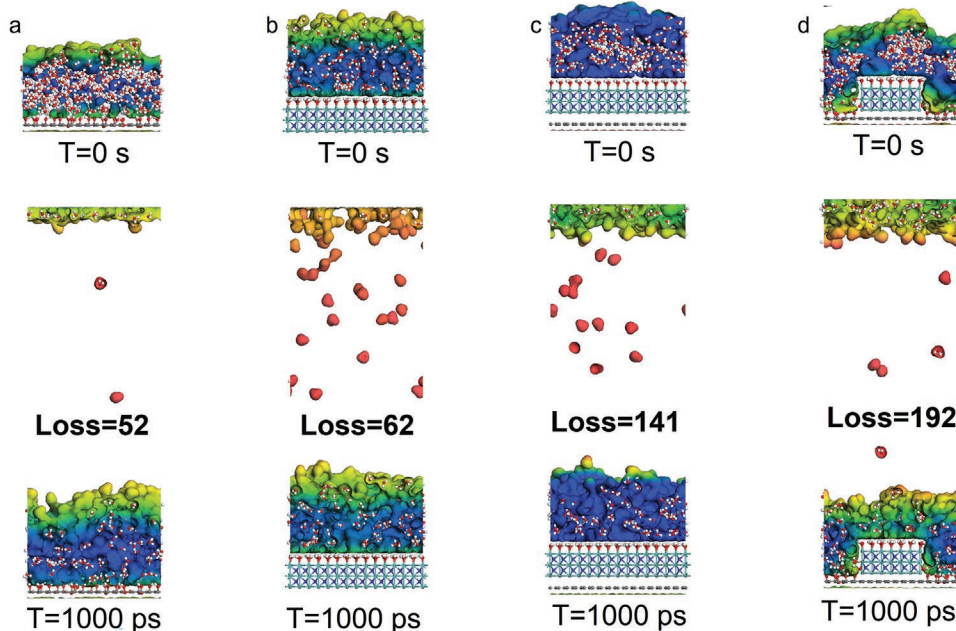


Figure 6. Simulation of water evaporation over different surfaces. Snapshots of water loss on a) rGO surface, b) MoN_{1.2} surface, c) MoN_{1.2}-rGO surface without exposed heterointerface, and d) MoN_{1.2}-rGO surface with heterointerface at 0 and 1000 ps, respectively.

interconnected pores in the hydrogel, which enabled fast salt ion diffusion back to the bulk water when the salt concentration on the evaporation surface increased during solar evaporation.^[60,61] The generated vapor was condensed and collected as clean water. The concentrations of Na⁺ (11.9 ppm), K⁺ (1.9 ppm), Ca²⁺ (0.2 ppm), and Mg²⁺ (0.6 ppm) in the collected water were much lower than the guideline salinity levels for drinkable desalination water defined by both World Health Organization (WHO) and US Environmental Protection Agency (USEPA),^[62] demonstrating the high quality of the water produced by solar evaporation (Figure S25b, Supporting Information).

3. Conclusion

In this work, 2D MoN_{1.2}-rGO-HSs with heterointerfaces have been successfully prepared as photothermal materials for highly efficient interfacial solar evaporation. The stacked 2D-2D structures and the formed heterointerfaces were confirmed by TEM, XPS and NEXAFS. The numerical simulation demonstrated that due to the closely stacked 2D structures and the heterointerfaces, the significant difference in MoN_{1.2}-water and rGO-water interactions effectively disturbed the hydrogen bonding network and produced more IW, which significantly lowered the evaporation enthalpy (from 2242 to 1062 kJ kg⁻¹) and accelerated water evaporation. Therefore, the MoN_{1.2}-rGO-HSs hydrogel achieved a high evaporation rate of 2.6 kg m⁻² h⁻¹, which exceeded the theoretical limit (≈1.46 kg m⁻² h⁻¹) of a typical 2D evaporator under 1.0 illumination and was also higher than that of reported TMNs-based evaporators. The finding of this work provides a promising strategy to design heterostructures to improve solar evaporation rate by tuning water hydrogen bonding state.

4. Experimental Section

Materials and Chemicals: PDDA solution (20 wt.% in H₂O), PVA, and tannic acid (TA) were purchased from Sigma-Aldrich. rGO was provided by Huasheng Graphite Co., Ltd, China. Unless otherwise indicated, Milli-Q water with a resistance >18.2 MΩ cm⁻¹ was used for all experiments.

Preparation of 2D MoN_{1.2} Nanosheets: The 2D MoN_{1.2} nanosheets were prepared according to the previously reported method.^[56] 1.44 g MoO₃ and 2.42 g Na₂MoO₄·2H₂O (molar ratio of 1:1) were first mixed via ball milling using a planetary micro mill system (Fritsch PULVERISETTE 7 premium line) at a rotation speed of 400 rpm for 20 min (two cycles). Then, 100 mg of the mixture was placed into a porcelain boat and annealed at 650 °C for 5 h at a ramp rate of 1 °C min⁻¹ under 5% NH₃ in Ar atmosphere. Finally, the 2D MoN_{1.2} nanosheets were obtained and freeze dried after removing the salt by filtration.

Preparation of rGO-PVA Hydrogel: 8 mg rGO was added into 2 mL mixed solvent of Milli-Q water and ethanol (7:1 v/v%) and sonicated for 1 h to form a rGO dispersion. Then, the dispersion was mixed with 15 mL PVA solution (15 wt.%) by magnetic stirring and heating at 80 °C for 20 mins to form the rGO-PVA mixture. The mixture was then poured into a cylindrical PTFE mold (diameter: 3 cm) placed on a copper block sitting in liquid nitrogen. After fully frozen, the mixture was freeze-dried for 24 h. Finally, the freeze-dried sample was immersed in TA aqueous solution (50 mg mL⁻¹) for 24 h to form TA crosslinked rGO-PVA hydrogel. The residual TA was removed from the hydrogel by washing with Milli-Q water for several times. The diameter of the obtained hydrogel was 2.9 cm, and the surface area was 6.60 cm².

Preparation of MoN_{1.2}-PVA Hydrogel: 75 mg MoN_{1.2} was added into 2 mL Milli-Q water and sonicated for 30 mins to form a MoN_{1.2} dispersion. Then, the dispersion was mixed with 15 mL PVA solution (15 wt.%) by magnetic stirring and heating at 80 °C for 20 mins to form the MoN_{1.2}-PVA mixture. The mixture was then poured into a cylindrical PTFE mold (diameter: 3 cm) placed on a copper block sitting in liquid nitrogen. After fully frozen, the mixture was freeze-dried for 24 h. Finally, the freeze-dried sample was immersed in TA aqueous solution (50 mg mL⁻¹) for 24 h to form TA cross-linked MoN_{1.2}-PVA hydrogel. The residual TA was removed from the hydrogel by washing with Milli-Q

water for several times. The diameter of the obtained hydrogel was 2.9 cm, and the surface area was 6.60 cm².

Preparation of MoN_{1.2}-rGO-PVA Hydrogel: 37.5 mg MoN_{1.2} and 4 mg rGO were added into 2 mL of Milli-Q water and ethanol (7:1 v/v%) and sonicated for 30 mins to form a MoN_{1.2}-rGO dispersion. Then, the dispersion was mixed with 15 mL PVA solution (15 wt.%) by magnetic stirring and heating at 80 °C for 20 mins to form the MoN_{1.2}-rGO-PVA mixture. The mixture was then poured into a cylindrical PTFE mold (diameter: 3 cm) placed on a copper block sitting in liquid nitrogen. After fully frozen, the mixture was freeze-dried for 24 h. Finally, the freeze-dried sample was immersed in TA aqueous solution (50 mg mL⁻¹) for 24 h to form TA cross-linked MoN_{1.2}-rGO-PVA hydrogel. The residual TA was removed from the hydrogel by washing with Milli-Q water for several times. The diameter of the obtained hydrogel was 2.9 cm, and the surface area was 6.60 cm².

Preparation of MoN_{1.2}-rGO-HSs-PVA Hydrogel: 4 mg rGO was added into 2 mL PDDA aqueous solution (60 mg mL⁻¹) and sonicated for 30 mins to form a rGO/PDDA dispersion. Then 37.5 mg MoN_{1.2} was added into the rGO/PDDA dispersion and sonicated for another 10 mins to form the rGO/PDDA/MoN_{1.2} dispersion. Thereafter, the dispersion was mixed with 15 mL PVA solution (15 wt.%) by magnetic stirring and heating at 80 °C for 20 mins to form the rGO/PDDA/MoN_{1.2}-PVA mixture. The mixture was then poured into a cylindrical PTFE mold (diameter: 3 cm) placed on a copper block sitting in liquid nitrogen. After fully frozen, the mixture was freeze-dried for 24 h. Finally, the freeze-dried sample was immersed in TA aqueous solution (50 mg mL⁻¹) for 24 h to form TA cross-linked MoN_{1.2}-rGO-HSs-PVA hydrogel. The residual TA was removed from the hydrogel by washing with Milli-Q water for several times. The diameter of the obtained hydrogel was 2.9 cm, and the surface area was 6.60 cm².

Characterizations: Zeta potential was measured using Malvern Zetasizer Nano ZS. The morphology and structure were analyzed by scanning electron microscopy (SEM, Zeiss Gemini 2), transmission electron microscopy (TEM, JEOL JEM-2100F and FEI Titan Themis 80–200), and X-ray diffraction (XRD, D8 Advance, Bruker) with Cu K α radiation ($\lambda = 1.5418 \text{ \AA}$). The composition and surface state were probed by X-ray photoelectron spectroscopy (XPS, Kratos AxisUltra XPS). The X-ray absorption fine structure (NEXAFS) measurements were performed on the soft X-ray spectroscopy beamline at the Australian Synchrotron, which was equipped with a hemispherical electron analyzer and a microchannel plate detector that enabled simultaneously recording of the total electron yield and partial electron yield. Hydrophilicity of the hydrogels was investigated by the sessile drop method (Dataphysics OCA 20). Light absorption spectra were measured using a UV-3600 Spectrometer (Shimadzu). ICP-OES (Agilent 7500) was used to measure the concentrations of ions. Raman spectroscopy was recorded by a confocal Raman microscope (Horiba LabRAM HR Evolution) with a 100 \times objective (Olympus). Heat flow was recorded by DSC analysis (TA instruments Discovery TGA/DSC).

Solar-Driven Steam Generation: Solar illumination was provided by a Newport Oriel Solar Simulator (Class ABA, 450 W, 69 920). The mass change of water/seawater was recorded by an electronic balance. The surface temperature of the evaporator was monitored by an IR camera (FLIR E64501). All the indoor test was proceeded in the lab with constant ambient temperature of $\approx 25 \text{ }^\circ\text{C}$ and humidity of $\approx 32\%$. The performance of water evaporation rate was calculated by the following formula:

$$R = \frac{M_c}{tS} \text{ (kg m}^{-2} \text{ h}^{-1}) \quad (1)$$

Where, R is the evaporation rate (kg m⁻² h⁻¹), M_c is the mass change during the evaporation, t is the evaporation time (h), and S is the area of the evaporation surface (m²).

Molecular Dynamics Simulation for Adsorption Behavior: The interactions between water molecules and rGO or MoN_{1.2} at the interfaces were studied by molecular dynamics simulation. The total kinetic time was 300 ps, with a time step of 1 ps. The first 150 ps was applied to reach the balance state. The interactions between water

molecules and the heterostructures were calculated from 150 to 300 ps. A total of 150 times of interactions were calculated and the average value was taken as the adsorption energy.

Molecular Dynamics Simulation for Evaporation Behavior: The evaporation of water was studied by molecular dynamics simulation. Forcite Plus module in Materials Studio was used to set up the pure water system and heterostructure-water systems through the Amorphous Cell module. The solution surface and heterostructure surface were spliced through build layer. The initial number of water molecules was 500. Before dynamic evaporation simulation, the model energy was minimized by geometric optimization. Among them, the force field was the Universal Force field, and the charge distribution method was QEQ assigned. In order to study the non-bonding interaction of the system, the used tracing electrostatic summations method was Ewald, and the van der Waals summations method was atom based. The temperature was set 310.5 K. The total kinetic time was 1000 ps, and the time step was 0.5 fs.

Supporting Information

Supporting Information is available from the Wiley Online Library or from the author.

Acknowledgements

H.Y. and D.W. contributed equally to this work. H.X. acknowledges the financial support from the Australian Research Council (FT190100485, DP220100583), P.W. acknowledges the financial support from China Scholarship Council for primary scholarships and from the Future Industries Institute for top up scholarships. X.Y. was supported by Science Fund for Distinguished Young Scholars (JC2019002), Nanjing Forestry University. All authors acknowledge the use of the SA node of the NCRIS-enabled Australian National Fabrication Facility (ANFF).

Open access publishing facilitated by University of South Australia, as part of the Wiley - University of South Australia agreement via the Council of Australian University Librarians.

Conflict of Interest

The authors declare no conflict of interest.

Data Availability Statement

The data that support the findings of this study are available from the corresponding author upon reasonable request.

Keywords

2D heterostructures, evaporation enthalpy, interfacial solar evaporation, molybdenum nitrides, reduced graphene oxides

Received: December 20, 2022

Revised: February 21, 2023

Published online: March 14, 2023

- [1] H. Jin, T. Song, U. Paik, S.-Z. Qiao, *Acc. Mater. Res.* **2021**, 2, 559.
- [2] H. Wang, J. Li, K. Li, Y. Lin, J. Chen, L. Gao, V. Nicolosi, X. Xiao, J.-M. Lee, *Chem. Soc. Rev.* **2021**, 50, 1354.

- [3] J. Ben, X. Liu, C. Wang, Y. Zhang, Z. Shi, Y. Jia, S. Zhang, H. Zhang, W. Yu, D. Li, X. Sun, *Adv. Mater.* **2021**, *33*, 2006761.
- [4] X. Xiao, H. Yu, H. Jin, M. Wu, Y. Fang, J. Sun, Z. Hu, T. Li, J. Wu, L. Huang, Y. Gogotsi, J. Zhou, *ACS Nano* **2017**, *11*, 2180.
- [5] H. Jin, X. Liu, A. Vasileff, Y. Jiao, Y. Zhao, Y. Zheng, S.-Z. Qiao, *ACS Nano* **2018**, *12*, 12761.
- [6] H. Yu, X. Yang, X. Xiao, M. Chen, Q. Zhang, L. Huang, J. Wu, T. Li, S. Chen, L. Song, L. Gu, B. Y. Xia, G. Feng, J. Li, J. Zhou, *Adv. Mater.* **2018**, *30*, 1805655.
- [7] Y. Guo, G. Yu, *ACS Mater. Lett.* **2022**, *4*, 713.
- [8] M. J. Margeson, M. Dasog, *Environ. Sci.: Water Res. Technol.* **2020**, *6*, 3169.
- [9] L. Zhu, L. Sun, H. Zhang, D. Yu, H. Aslan, J. Zhao, Z. Li, M. Yu, F. Besenbacher, Y. Sun, *Nano Energy* **2019**, *57*, 842.
- [10] L. Wang, J. Shang, G. Yang, Y. Ma, L. Kou, D. Liu, H. Yin, D. Hegh, J. Razal, W. Lei, *Small* **2022**, *18*, 2201770.
- [11] Y. Zhou, T. Ding, M. Gao, K. H. Chan, Y. Cheng, J. He, G. W. Ho, *Nano Energy* **2020**, *77*, 105102.
- [12] T. Ding, G. W. Ho, *Joule* **2021**, *5*, 1639.
- [13] X. Chen, S. He, M. M. Falinski, Y. Wang, T. Li, S. Zheng, D. Sun, J. Dai, Y. Bian, X. Zhu, J. Jiang, L. Hu, Z. J. Ren, *Energy Environ. Sci.* **2021**, *14*, 5347.
- [14] M. Jiao, Y. Yao, C. Chen, B. Jiang, G. Pastel, Z. Lin, Q. Wu, M. Cui, S. He, L. Hu, *ACS Mater. Lett.* **2020**, *2*, 430.
- [15] M. Zou, Y. Zhang, Z. Cai, C. Li, Z. Sun, C. Yu, Z. Dong, L. Wu, Y. Song, *Adv. Mater.* **2021**, *33*, 2102443.
- [16] L. Wu, Z. Dong, Z. Cai, T. Ganapathy, N. X. Fang, C. Li, C. Yu, Y. Zhang, Y. Song, *Nat. Commun.* **2020**, *11*, 521.
- [17] T. Li, Q. Fang, J. Wang, H. Lin, Q. Han, P. Wang, F. Liu, *J. Mater. Chem. A* **2021**, *9*, 390.
- [18] C. Zhang, Y. Shi, L. Shi, H. Li, R. Li, S. Hong, S. Zhuo, T. Zhang, P. Wang, *Nat. Commun.* **2021**, *12*, 998.
- [19] S. Ishii, R. P. Sugavaneshwar, T. Nagao, *J. Phys. Chem. C* **2016**, *120*, 2343.
- [20] F. Zhao, X. Zhou, Y. Shi, X. Qian, M. Alexander, X. Zhao, S. Mendez, R. Yang, L. Qu, G. Yu, *Nat. Nanotechnol.* **2018**, *13*, 489.
- [21] X. Zhou, F. Zhao, Y. Guo, B. Rosenberger, G. Yu, *Sci. Adv.* **2019**, *5*, eaaw5484.
- [22] Z. Yu, R. Gu, Y. Tian, P. Xie, B. Jin, S. Cheng, *Adv. Funct. Mater.* **2022**, *32*, 2108586.
- [23] Y. Lu, D. Fan, Z. Shen, H. Zhang, H. Xu, X. Yang, *Nano Energy* **2022**, *95*, 107016.
- [24] X. Min, B. Zhu, B. Li, J. Li, J. Zhu, *Acc. Mater. Res.* **2021**, *2*, 198.
- [25] X. Ye, L.-H. Chung, K. Li, S. Zheng, Y.-L. Wong, Z. Feng, Y. He, D. Chu, Z. Xu, L. Yu, J. He, *Nat. Commun.* **2022**, *13*, 6116.
- [26] Y. Li, Y. Ma, Y. Liao, L. Ji, R. Zhao, D. Zhu, X. Hu, G. Qin, H. Rong, X. Zhang, *Adv. Energy Mater.* **2022**, *12*, 2203057.
- [27] P. Liu, Y.-b. Hu, X.-Y. Li, L. Xu, C. Chen, B. Yuan, M.-L. Fu, *Angew. Chem., Int. Ed.* **2022**, *61*, e202208587.
- [28] L. Pu, H. Ma, J. Dong, C. Zhang, F. Lai, G. He, P. Ma, W. Dong, Y. Huang, T. Liu, *Nano Lett.* **2022**, *22*, 4560.
- [29] Y. Zhang, Y. Wang, B. Yu, K. Yin, Z. Zhang, *Adv. Mater.* **2022**, *34*, 2200108.
- [30] X. Li, W. Xie, J. Zhu, *Adv. Sci.* **2022**, *9*, 2104181.
- [31] S. Fang, W. Chu, J. Tan, W. Guo, *Nano Energy* **2022**, *101*, 107605.
- [32] Y. Wang, X. Wu, P. Wu, H. Yu, J. Zhao, X. Yang, Q. Li, Z. Zhang, D. Zhang, G. Owens, H. Xu, *J. Mater. Chem. A* **2022**, *10*, 14470.
- [33] T. Gao, Y. Wang, X. Wu, P. Wu, X. Yang, Q. Li, Z. Zhang, D. Zhang, G. Owens, H. Xu, *Sci. Bull.* **2022**, *67*, 1572.
- [34] Y. Wang, X. Wu, P. Wu, J. Zhao, X. Yang, G. Owens, H. Xu, *Sci. Bull.* **2021**, *66*, 2479.
- [35] Y. Guo, X. Zhou, F. Zhao, J. Bae, B. Rosenberger, G. Yu, *ACS Nano* **2019**, *13*, 7913.
- [36] Y. Lu, D. Fan, Y. Wang, H. Xu, C. Lu, X. Yang, *ACS Nano* **2021**, *15*, 10366.
- [37] H.-Y. Zhao, J. Huang, J. Zhou, L.-F. Chen, C. Wang, Y. Bai, J. Zhou, Y. Deng, W.-X. Dong, Y.-S. Li, S.-H. Yu, *ACS Nano* **2022**, *16*, 3554.
- [38] X. Lin, P. Wang, R. Hong, X. Zhu, Y. Liu, X. Pan, X. Qiu, Y. Qin, *Adv. Funct. Mater.* **2022**, *32*, 2209262.
- [39] X. Chen, N. Yang, Y. Wang, H. He, J. Wang, J. Wan, H. Jiang, B. Xu, L. Wang, R. Yu, L. Tong, L. Gu, Q. Xiong, C. Chen, S. Zhang, D. Wang, *Adv. Mater.* **2022**, *34*, 2107400.
- [40] Y. Guo, C. M. Dundas, X. Zhou, K. P. Johnston, G. Yu, *Adv. Mater.* **2021**, *33*, 2102994.
- [41] X. Yan, S. Lyu, X.-Q. Xu, W. Chen, P. Shang, Z. Yang, G. Zhang, W. Chen, Y. Wang, L. Chen, *Angew. Chem., Int. Ed.* **2022**, *61*, e202201900.
- [42] X. Mu, J. Zhou, P. Wang, H. Chen, T. Yang, S. Chen, L. Miao, T. Mori, *Energy Environ. Sci.* **2022**, *15*, 3388.
- [43] A. LaPotin, Y. Zhong, L. Zhang, L. Zhao, A. Leroy, H. Kim, S. R. Rao, E. N. Wang, *Joule* **2021**, *5*, 166.
- [44] C. Li, S. Cao, J. Lutzki, J. Yang, T. Konegger, F. Kleitz, A. Thomas, *J. Am. Chem. Soc.* **2022**, *144*, 3083.
- [45] Y. Guo, F. Zhao, X. Zhou, Z. Chen, G. Yu, *Nano Lett.* **2019**, *19*, 2530.
- [46] Y. Hu, H. Ma, M. Wu, T. Lin, H. Yao, F. Liu, H. Cheng, L. Qu, *Nat. Commun.* **2022**, *13*, 4335.
- [47] Y. Liu, N. O. Weiss, X. Duan, H.-C. Cheng, Y. Huang, X. Duan, *Nat. Rev. Mater.* **2016**, *1*, 16042.
- [48] K. S. Novoselov, A. Mishchenko, A. Carvalho, A. H. Castro Neto, *Science* **2016**, *353*, aac9439.
- [49] Y. Li, J. Zhang, Q. Chen, X. Xia, M. Chen, *Adv. Mater.* **2021**, *33*, 2100855.
- [50] A. S. Mayorov, R. V. Gorbachev, S. V. Morozov, L. Britnell, R. Jalil, L. A. Ponomarenko, P. Blake, K. S. Novoselov, K. Watanabe, T. Taniguchi, A. K. Geim, *Nano Lett.* **2011**, *11*, 2396.
- [51] L. Wang, D. Liu, L. Jiang, Y. Ma, G. Yang, Y. Qian, W. Lei, *Nano Energy* **2022**, *98*, 107192.
- [52] L. Zhang, Y. Zhong, X. Qian, Q. Song, J. Zhou, L. Li, L. Guo, G. Chen, E. N. Wang, *ACS Appl. Mater. Interfaces* **2021**, *13*, 46055.
- [53] Y. Shi, R. Li, Y. Jin, S. Zhuo, L. Shi, J. Chang, S. Hong, K.-C. Ng, P. Wang, *Joule* **2018**, *2*, 1171.
- [54] X. Li, J. Li, J. Lu, N. Xu, C. Chen, X. Min, B. Zhu, H. Li, L. Zhou, S. Zhu, T. Zhang, J. Zhu, *Joule* **2018**, *2*, 1331.
- [55] H. Song, Y. Liu, Z. Liu, M. H. Singer, C. Li, A. R. Cheney, D. Ji, L. Zhou, N. Zhang, X. Zeng, Z. Bei, Z. Yu, S. Jiang, Q. Gan, *Adv. Sci.* **2018**, *5*, 1800222.
- [56] H. Jin, Q. Gu, B. Chen, C. Tang, Y. Zheng, H. Zhang, M. Jaroniec, S.-Z. Qiao, *Chem* **2020**, *6*, 2382.
- [57] E. J. Lede, F. G. Requejo, B. Pawelec, J. L. G. Fierro, *J. Phys. Chem. B* **2002**, *106*, 7824.
- [58] T. Gao, X. Wu, Y. Wang, G. Owens, H. Xu, *Sol. RRL* **2021**, *5*, 2100053.
- [59] B. Shao, Y. Wang, X. Wu, Y. Lu, X. Yang, G. Y. Chen, G. Owens, H. Xu, *J. Mater. Chem. A* **2020**, *8*, 11665.
- [60] Z. Yu, R. Gu, Y. Zhang, S. Guo, S. Cheng, S. C. Tan, *Nano Energy* **2022**, *98*, 107287.
- [61] W. Zhou, C. Zhou, C. Deng, L. Chen, X. Zeng, Y. Zhang, L. Tan, B. Hu, S. Guo, L. Dong, S. C. Tan, *Adv. Funct. Mater.* **2022**, *32*, 2113264.
- [62] L. Zhou, Y. Tan, J. Wang, W. Xu, Y. Yuan, W. Cai, S. Zhu, J. Zhu, *Nat. Photon.* **2016**, *10*, 393.